Esa Kostamo
Aalto University School of Engineering,
Sähkömiehentie 4,
Espoo 02150, Finland
e-mail: esa.kostamo@aalto.fi

Michele Focchi
e-mail: michele.focchi@iit.it

Emanuele Guglielmino
e-mail: emanuele.guglielmino@iit.it

Department of Advanced Robotics,
Istituto Italiano di Tecnologia,
Morego 30,
Genova 16163, Italy

Jari Kostamo
Aalto University School of Engineering,
Sähkömiehentie 4,
Espoo 02150, Finland
e-mail: jari.kostamo@aalto.fi

Claudio Semini
Department of Advanced Robotics,
Istituto Italiano di Tecnologia,
Morego 30,
Genova 16163, Italy
e-mail: claudio.semini@iit.it

Jonas Buchli
Institute of Robotics and Intelligent Systems,
ETH Zurich, Tannenstr. 3,
Zürich 8092, Switzerland
e-mail: buchlij@ethz.ch

Matti Pietola
Aalto University School of Engineering,
Otakaari 4,
Espoo 02150, Finland
e-mail: matti.pietola@aalto.fi

Darwin Caldwell
Department of Advanced Robotics,
Istituto Italiano di Tecnologia,
Morego 30,
Genova 16163, Italy
e-mail: darwin.caldwell@iit.it

Magnetorheologically Damped Compliant Foot for Legged Robotic Application

This paper presents an innovative solution for bounce reduction between a robotic leg and the ground by means of a semi-active compliant foot. The aim of this work is to enhance the controllability and the balance of a legged robot by improving the traction between the foot tip and the ground. The compliant foot is custom-designed for quadruped walking robots and it consists of a linear spring and a magnetorheological (MR) damper. By utilizing magnetorheological technology in the damper element, the damping coefficient of the compliant foot can be altered across a wide range without any additional moving parts. The content of this paper is twofold. In the first part the design, a prototype and a model of the semi-active compliant foot are presented, and the performance of the magnetorheological damper is experimentally studied in quasi-static and dynamic cases. Based on the quasi-static measurements, the damping force can be controlled in a range from 15 N to 310 N. From the frequency response measurements, it can be shown that the controllable damping force has a bandwidth higher than 100 Hz. The second part of this paper presents an online stiffness identification algorithm and a mathematical model of the robotic leg. A critical damping control law is proposed and implemented in order to demonstrate the effectiveness of the device that makes use of smart materials. Further on, drop tests have been carried out to assess the performance of the proposed control law in terms of bounce reduction and settling time. The results demonstrate that by real-time control of the damping force 98% bounce reduction with settling time of 170 ms can be achieved. [DOI: 10.1115/1.4025966]

Keywords: magnetorheological, damping, bouncing reduction, energy dissipation, semi-active, robotic leg

1 Introduction

In industrial robotic applications, engineers have traditionally striven to maximize the stiffness of the robotic arms. This kind of trend is well justified since an increment in stiffness improves the precision, stability, and bandwidth of position-control without compromising the stability of the system. However, in these applications, the operating environment of the robot is precisely known and the mechanical design and the controller parameters can be finely tuned to meet the design target.

Another class of robotic machines is biomimetic robots. By definition, biomimetic robots mimic the structure and movement of humans and animals [1]. Such robots are often designed to operate in unstructured environment, where joint compliance plays a major role [2]. In particular, compliant legged robots have the potential to walk or run through uneven and possibly unknown environments.

To achieve robust legged locomotion over difficult terrains, different control approaches are required from just high-gain position control. Such robots exhibit a very stiff disturbance rejection behavior and are therefore not well suited to deal with unstructured environments in the real world outside the laboratory. In these applications, it is better to use a force control algorithm, allowing the robot to adapt to changing environments or to react smoothly to unexpected obstacles and forces. To control the

interaction forces, a lot of different approaches can be implemented which might be good candidates to fulfill the requirements set by the control system [1]. On the other hand, the performance of these approaches is limited by the actuator dynamics. Bandwidth limitations create difficulties in damping out impact forces and abrupt contacts with the environment. In general, a force feedback system, in which a rigid body and a stiff load cell are combined, has several shortcomings. In a load cell, even a small movement causes high feedback force value resulting in a strong control action in a high-gain controller. This could result in instability and chatter when the robot makes contact with a stiff environment. To remove the chatter, lower gain values should be used, causing a slower response from the robotic actuator. This problem can be addressed actively by controlling the compliance with impedance control. However, the impact forces usually have high frequency content and there are bandwidth limitations present in the controller (the range of frequency, where impedance is tracked is limited). Therefore, a certain amount of compliance is still necessary to filter the force components which are out of the bandwidth impedance controller. Differently, high peak force would be transmitted to the mechanical structure. This could lead to damage to the weakest components (e.g., bearings, load cells, gearboxes) and, over time, to fatigue fractures [3].

To overcome this challenge, a lot of effort has been invested in studying different kinds of passive compliant actuators for robotic applications in order to decouple the robot's inertia from the environment. So far, many variations and concepts of elastic or compliant actuators have been presented. Pratt et al. introduced a concept of series elastic actuators (SEA) that essentially consists of a linear spring in series with a stiff actuator [4]. The SEA meets the benefits listed above but the compliance of the actuator is determined by the spring constant and therefore cannot be adjusted during the operation. The ability to change the joint stiffness is desirable in robotic applications because this enables to change the dynamics of a robot. The concept of variable stiffness actuator (VSA) was described by Tonietti et al. [5]. Their mechanism is based on a spring-pulley-belt system which has a more complex nonlinearity of the output force compared to many other designs. On the other hand, the more compact size of the VSA can be considered as an advantage. Another approach in realizing an elastic actuator is the actuator with mechanically adjustable series compliance (AMASC) developed by Hurst et al. [6]. The mechanism of the AMASC is based on multiple pulleys and cables which makes it complex but the advantage is that only one actuator is needed to control the compliance or equilibrium position.

Perhaps, the most organic imitation of a muscle can be found in pneumatic artificial muscles (PAM). Pressurizing the PAM expands the actuator radially creating an axial force. The pressurized air inside the PAM makes the actuator inherently compliant, behaving in a tendon-like fashion. The most well-known PAM design is the McKibben muscle [7]. The braided mesh structure of the muscle creates high stiffness in the axial direction but also notable hysteresis to the force output of the actuator that causes problems to control. In their study, Verrelst et al. implemented pleated pneumatic artificial muscles in the biped robot Lucy [8]. With pleated design, the hysteresis in the force output can be significantly reduced enabling more accurate force control. Even more precise reproduction of a musclotendon-like actuator was proposed by Klute et al. [9]. In their study, two pneumatic artificial muscles were used as a contracting elements and a passive hydraulic damper was mounted parallel with the muscles in order to attain desired force-velocity properties for the actuator. As an artificial tendon, two linear springs were utilized in series with the pneumatic muscles and the damper. Experimental results showed that the actuator-damper-tendon system behaved in a muscle and tendon-like manner.

In comparison to series elastic actuators, Chee–Meng et al. proposed a concept of series damper actuator (SDA) [10]. In their study, the experimental setup consisted of an electric motor, a rotational MR damper (Lord MRB-2107-3), a load and necessary sensors to measure the torque and angular velocities before and after the magnetorheological damper. As an advantage, the damping coefficient of the system can be continuously controlled enabling high torque fidelity at both high and low torque ranges. The SDA has inherent impact absorption properties that are very important for walking robots, haptic devices or robot manipulators. The main disadvantage of the SDA is related to its energy dissipation properties. The SDA application can only dissipate energy from the system since there is no energy conserving elastic component. The experimental results demonstrated that the SDA can be controlled to have a linear torque versus velocity relationship with varying damping coefficient.

The variable physical damping actuator (VPDA) for robotic applications was studied by Laffranchi et al. [11]. In their study, the rotational VPDA unit consisted of piezoelectric actuated friction damper and a passive torsion spring element coupled in parallel to the damper. The advantages compared to other semi-active damping technologies are its compact and light weight structure, cleanliness and simple mechanical design. The experimental results demonstrated that the VPDA can be an effective means of damping the oscillations in rotational robotic joints. A control law for VPDA was proposed showing that different damping ratios could be replicated with good fidelity.

The objective of this study is to improve foot contact of a legged robot with the ground by combining a magnetorheological damping element with a linear spring to create a semi-active compliant robotic foot. The main drawback of passive compliant elements is that chatter/bouncing between the foot tip and the ground can occur and thus traction can be temporarily lost. The energy stored in a spring, that can generate bouncing, can be dissipated by using a passive damping element but on the other hand a passive damper would perform a critically damped response only for a particular combination of robot masses and spring constants. With regard to the balance control of the quadruped robot HyQ [12,13], reduced bouncing and improved ground contact are crucial since robot posture can only be adjusted during the stance phase. In some operating conditions, it can also be beneficial, from an energy efficiency point of view, to have as low damping coefficient as possible. Therefore, it is worth investigating the feasibility of using controlled semi-active damping [14] in order to reduce robot bouncing induced by the impact forces at touch-down.

By utilizing the MR technology, the damping force of the novel compliant foot presented in this paper can be controlled in a range that goes from ten up to hundreds of Newtons with a bandwidth of 100 Hz. The fast response of the prototype MR damper enables a real-time control of the damping force and therefore appropriate control algorithms can be activated during the stance phase, which in normal trotting for HyQ usually varies in a range of 100–300 ms depending on the gait parameters. By applying different control algorithms, the damper can emulate the operation of a conventional viscous damper with controllable damping factor, a negative spring, a constant friction force or any combination thereof.

2 Magnetorheological Compliant Foot

2.1 Magnetorheological Fluids. Magnetorheological fluids belong to the group of smart materials whose characteristic properties can be altered by an external magnetic field. MR fluids essentially consist of micron-sized magnetisable particles in a low viscosity carrier fluid. The functional principle of the fluid is based on the alignment of the ferromagnetic particles along the magnetic flux lines. The particle chains increase the yield stress of the fluid and by the applied magnetic field the fluid flow can be resisted or totally restricted [15]. By utilizing this mechanism, the characteristic properties of an MR device can be altered in a wide range without any moving or wearing parts.

MR fluids can be considered as an interesting technology for highly dynamic applications. In the literature, it has been reported that the response time for the alignment of the particles in MR
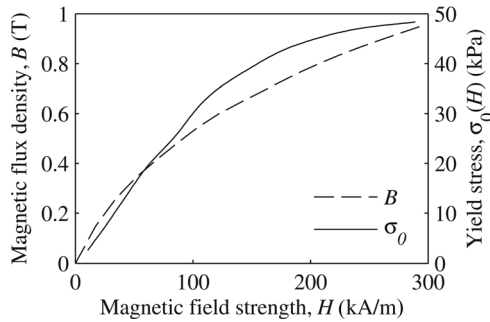
Fig. 1 MRF-132DG magnetization characteristic curve [18] and yield stress as a function of magnetic field strength

Weight	1.1 kg
Total length	232 mm
Stroke	34 mm
Largest diameter	49 mm
Cylinder inner diameter	26 mm
Piston diameter	25 mm
Fluid gap	0.5 mm
Spring constant	15.8 N/mm
Number of Ampere turns in the coil	80
Max damping force (@4 A electric current)	485 N
Operating bandwidth, −3 dB limit	>100 Hz
Max input power	<4 W

fluid is less than 0.5 ms [16]. It has also been shown that a damper in the range of kN damping force can be constructed to operate within a response time of 2 ms [17].

The MR fluid used in this study is the MRF-132DG (Lord Corporation, Cary, North Carolina, United States). It is a hydrocarbon based fluid that has a high resistance to hard settling and is developed for energy dissipative applications. For this fluid, the magnetization characteristic curve and yield stress as a function of magnetic field strength are presented in Fig. 1.

2.2 Construction of the Magnetorheological Compliant Foot. The construction of the magnetorheological compliant foot prototype is presented in Fig. 2 with a cross-section view of the computer aided design (CAD) in which the main functional components are numbered and pointed out. The end caps (4) and (12) are machined of aluminum and the material of the piston shaft (3) is surface hardened steel guide bar. Magnetically active parts in the construction are the piston (10) and the cylinder (11) which are manufactured of magnetically soft iron. The coil (9) around the piston is wound using 0.4 mm enameled copper wire.

The MR compliant foot is assembled as shown in Fig. 2 and the volume inside the cylinder is filled with magnetorheological fluid. The piston is manufactured to have a 1 mm smaller diameter in relation to the inner diameter of the cylinder tube. This difference forms a 0.5 mm annular fluid gap between the piston and the cylinder which enables the MR fluid to flow from one side of the piston to the other when the compliant foot is compressed or extended. Since the hydraulic components of the damper are designed to be symmetric, no gas reservoir is needed to compensate the movement of the piston.

The solenoid around the piston is used to generate the magnetic field between the piston and the cylinder. When electric current is applied, magnetic flux circulates in-between the piston and the cylinder tube over two fluid gaps (8) and creates the increase in the MR fluid's yield stress. This restricts the fluid flow over the piston generating a pressure difference over the piston and consequently generating a damping force when the piston shaft is

moved. The key parameters of the magnetorheological compliant foot are listed in Table 1.

3 Model of the Magnetorheological Damper

This section focuses on the modeling of the magnetorheological damper within the compliant foot. When formulating the model of the controllable damping force, the spring force is not taken into account in order to purely focus on the damping force generated by the semi-active damper.

3.1 Magnetic Model of the Magnetorheological Damper. The magnetic properties of the MR damper were estimated by using Finite Element Method Magnetics (FEMM) software. In the FEMM software, the nonlinear magnetic properties of the MR fluid (Fig. 1) can be taken into account and the intensity of the magnetic field in the fluid gap can be assessed using different values of electric current. For the magnetic performance of the MR damper, it was outlined that the magnetically active core parts (i.e., the piston and the cylinder), should not saturate when a two Ampere electric current is applied to the 80 turn solenoid.

In the FEMM model, the maximum size of the triangular mesh in the MR fluid (7) and the cylinder (11) was set to 0.05 mm (average height of the element) and in the piston (10) an element size of 0.5 mm was used. In these magnetically active details, finer mesh size was used in order to ensure adequate number of elements so that the number of elements does not have an effect to the modeling accuracy. In the air and the piston shaft (3), an automatic element size was selected in which case the software matches the element size in the interface of two bodies and increases the element size with distance from the interface.

Figure 3 presents the magnetic flux density distribution of the solved MR damper FEMM model at an electric current of 2 A. The dashed line (16) crossing through the MR fluid gaps (8) illustrates a line along which the strength of the magnetic field in the MR fluid has been analyzed. The analysis of the magnetic field strength begins 2 mm before the left sided MR fluid gap,
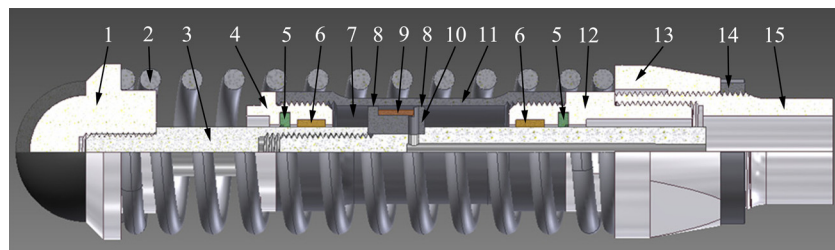

Fig. 2 CAD cross-section view of the MR foot. Numbered components: (1) rubber coated foot tip, (2) spring, (3) piston shaft, (4) lower end cap, (5) seal, (6) sliding bushing, (7) MR fluid, (8) MR fluid gap, (9) solenoid, (10) piston, (11) cylinder, (12) upper end cap, (13) spring precompression adjustment nut, (14) spring precompression locking nut, (15) mounting component to the robotic leg.
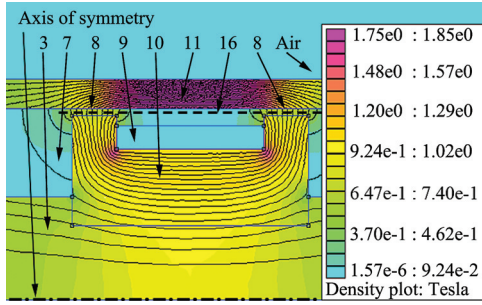
Fig. 3 Solved FEMM model of the core parts of the magneto-rheological damper at an electric current of 2 A. Numbered details: (3) piston shaft, (7) MR fluid, (8) MR fluid gap, (9) solenoid, (10) piston, (11) cylinder, (16) an illustration of the element that has been used to analyze the magnetic field strength distribution over the both MR fluid gaps. The numbering is equivalent with Fig. 2.

continuing over the piston and ends 2 mm after the right sided MR fluid gap.

Figure 4 shows the simulated responses of the magnetic field strength in the MR fluid gap at four different electric currents. The vertical dashed lines define the edges of the MR fluid gaps that are shown in Figs. 2 and 3. The simulated results show that the deviation of the magnetic field strength in the fluid gap is very flat and the increase in the magnetic field strength from 0 to 1 A and 1 to 2 A can be found approximately equal which indicates that no saturation occurs in the core material. With electric currents above 2 A, the core parts of the damper begin to saturate, which can be seen as a decreased increment in the magnetic field strength when the electric current is increased by 1 A. It is also worth noting that with electric currents above 2 A, the magnetic flux begins to leak outside of the MR fluid gap due to the saturation of the core material. In the middle of the piston, i.e., position between 5 mm and 15 mm, the magnetic field strength increases significantly at higher than 2 A electric currents, making also this area of the piston significant when simulating the quasi-static force response of the damper.

3.2 Quasi-Static Model. In this study, a third order polynomial model for annular flow channel is used to describe the static characteristics of the MR damper [19]. The derivation of the third order model begins by assumption that the fluid properties are independent of time in which case the rheological equation relating shear stress and shear rate can be written as

$$\dot{\gamma}_r = f(\sigma_r) \tag{1}$$

where r is the distance from the center axis of the fluid gap, σ_r is the shear stress, and $\dot{\gamma}_r$ is the shear rate of the fluid at the distance
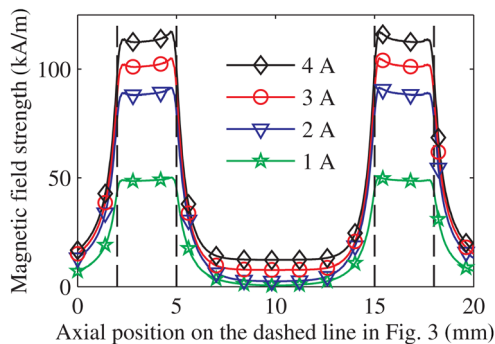

Fig. 4 Simulated magnetic field strengths on the dashed line (16) in Fig. 4. Simulations are calculated with four different electric currents.
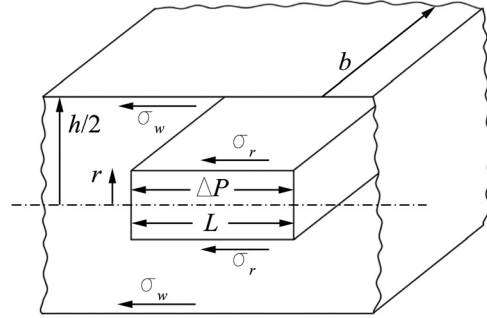
Fig. 5 The balance of forces on a symmetrically locating rectangular fluid element with total height of 2 r, length of L, and width of b. In this illustration, h is the total height of the fluid gap, ΔP is the pressure difference over the fluid element, σ_r is the shear stress at the surface of the fluid element and σ_w is the shear stress at the wall of the fluid gap.

of r from the center axis (see Fig. 5). For fluid flow in a rectangular fluid gap, Eq. (1) becomes

$$\frac{-du}{dr} = f(\sigma_r) \tag{2}$$

where u is the flow velocity.

The balance of forces on a symmetrically locating fluid element in a rectangular flow channel is illustrated in Fig. 5. In the derivation of the balance of forces, it is assumed that the annular flow channel can be simplified as a rectangular flow channel since the radial distance from the center axis of the MR damper to the center line of the flow channel is 26 times larger than the height of the flow channel. In this case, the curvature of the flow channel can be considered negligible in relation to the height of the flow channel. Also since the shape of the flow channel is annular, the front and the back surfaces of the fluid element in Fig. 5 are face to face in which case the effect of these surfaces to the force balance of the fluid element can be left out of the consideration. The pressure difference and shear stress over the fluid element gives

$$2bL\sigma_r = 2rb\Delta P \tag{3}$$

where b is the width of the flow channel, L is the length of the flow channel and ΔP is the pressure difference over the fluid element. Respectively, at the wall of the flow channel the balance of forces can be written as

$$2bL\sigma_w = hb\Delta P \tag{4}$$

where σ_w is the shear stress of the fluid at the wall of the flow channel and h is the height of the flow channel. By combining Eqs. (3) and (4) and substituting the result into Eq. (2), the velocity profile characteristic equation becomes

$$\frac{-du}{dr} = f\left(\frac{2\sigma_w r}{h}\right) \tag{5}$$

In the derivation of the final model for the MR damper, it is assumed that there is no slip at the walls of the flow channel in which case $u(h/2) = 0$. By taking the no-slip condition into account, the integration of Eq. (5) results

$$u(r) = \int_r^{h/2} f\left(\frac{2\sigma_w r}{h}\right) dr \tag{6}$$

Further on, the volume flow Q in a rectangular flow channel can be integrated as

$$Q = 2b \int_0^{h/2} u(r) \, dr \tag{7}$$

By integrating Eq. (7) by parts, it is obtained

$$Q = 2b \left[\Big._0^{h/2} \left[ru(r) - \int (r \, du(r)) \right] \right] \tag{8}$$

which combined with Eq. (6) results

$$Q = 2b \int_0^{h/2} rf \left(\frac{2\sigma_w r}{h} \right) dr \tag{9}$$

The combination of Eqs. (3) and (4) gives

$$r = \frac{\sigma_r h}{2\sigma_w} \tag{10}$$

When substituting Eq. (10) into Eq. (9), the volume flow in a rectangular flow gap as a function of the shear stress σ_r can be written as

$$Q = \frac{bh^2}{2\sigma_w^2} \int_0^{\sigma_w} \sigma_r f(\sigma_r) \, d\sigma_r \tag{11}$$

The magnetic field dependent rheological characteristics of MR fluids are often modeled by using Bingham plasticity equation. In this equation, the total shear stress of the fluid is divided into magnetic field strength and passive viscosity dependent components. For a Bingham plastic fluid, Eq. (1) is discontinuous and is given by

$$\begin{aligned} f(\sigma_r) &= 0 = \dot{\gamma}_r \, ; & 0 < \sigma_r < \sigma_0(H) \\ f(\sigma_r) &= \frac{\sigma_r - \sigma_0(H)}{\eta} = \dot{\gamma}_r \, ; & \sigma_0(H) < \sigma_r < \sigma_w \end{aligned} \tag{12}$$

where $\sigma_0(H)$ is the magnetic field dependent yield stress [15]. The field independent viscosity is represented by η that is $0.112 \, \mathrm{Pa \, s}$ according to the fluid manufacturer's specification [18]. Substituting Eq. (12) into Eq. (11) the equation for volume flow becomes

$$Q = \frac{bh^2}{2\eta\sigma_w^2} \int_{\sigma_0(H)}^{\sigma_w} \left[\sigma_r^2 - \sigma_r\sigma_0(H) \right] \, d\sigma_r \tag{13}$$

which after integration and substitution of σ_w from Eq. (4) gives

$$Q = \frac{bh^3 \Delta P}{12\eta L} \left[4 \left(\frac{L}{h\Delta P} \right)^3 \sigma_0(H)^3 - 3 \left(\frac{L}{h\Delta P} \right) \sigma_0(H) + 1 \right] \tag{14}$$

The shape of flow channel in the MR damper is annular and the height of the channel is defined by the radial gap between the piston and the cylinder. The width of the fluid gap is calculated by

$$b = \pi d \tag{15}$$

where d is the diameter of the piston in the MR damper. Substituting Eq. (15) into Eq. (14) and rearranging the terms, the final third order model of the MR damper can be written as

$$4 \left(\frac{L}{h\Delta P_{\mathrm{tot}}} \right)^3 \sigma_0(H)^3 - 3 \left(\frac{L}{h\Delta P_{\mathrm{tot}}} \right) \sigma_0(H) + \left(1 - \frac{12\eta L Q}{\pi d h^3 \Delta P_{\mathrm{tot}}} \right) = 0 \tag{16}$$

where ΔP_{tot} is now the total pressure difference over the piston inside the MR damper. The solution of this equation for the total

pressure difference can be found by numerical iteration. Of the three possible roots of this equation, two are inadmissible leaving the largest positive root as the only possible solution with physical meaning.

Once the pressure difference at certain intensity of magnetic field and volume flow has been solved, it is straightforward to estimate the total force produced by the MR damper. By taking the friction force into account, the total force F of the MR damper can be formulated as

$$F = \Delta P_{\mathrm{tot}} A + F_\mu = F_H + F_\eta + F_\mu \tag{17}$$

where A is the effective piston area, F_μ is the friction force due to the seals and the sliding bushings, F_H is the magnetic field controllable force, and F_η is the viscous force.

The total pressure difference can be analyzed as combination of the magnetic field dependent component ΔP_H and the postyield plastic viscosity component ΔP_η of the fluid. Hence, the total damping force can be decomposed into a magnetic field controllable force F_H and uncontrollable viscous force F_η and friction forces F_μ.

3.3 Dynamic Range. The magnetic field controllable force F_H and the dynamic range D are two important characteristics when defining the static performance of an MR damper. From the system dynamics point of view, it is desirable that an MR damper introduces as small force as possible to a system when it is turned off. On the other hand, when the MR damper is turned on the damper should be able to generate as high damping force as possible so that the dynamics of the system can be influenced in the widest possible range. This range of damping force between off-state and on-state is defined as dynamic range D that can be calculated as a ratio between the damper total force F and the uncontrollable force F_{uc} and can be written as [19]

$$D = \frac{F}{F_{\mathrm{uc}}} = 1 + \frac{F_H}{F_\eta + F_\mu} \tag{18}$$

4 Performance of the Magnetorheological Damper

This section presents quasi-static and dynamic performance measurements obtained with the MR damper.

4.1 Experimental Setup. The quasi-static and dynamic performance of the MR damper was identified by using an Easydur MZ3 material testing device (Easydur stress–strain machine, Italy). In these experiments, the magnetorheological compliant foot was mounted to the stress–strain machine without the spring in order to be able to study only the characteristic properties of the MR damper. The piston shaft of the damper was fixed to the moving cross head and the cylinder with mounting component were fixed via load cell to the lower cross head. The load cell was used to measure the total damping force at certain applied electric currents and displacement speeds. With two pressure sensors, it was possible to measure MR fluid pressure at the both sides of the piston. The stress–strain machine setup is illustrated in Fig. 6.

4.2 Friction Force Identification. The friction force in Eq. (17) was defined empirically. To study the friction force as a function of the applied electric current the MR fluid pressures were measured from the both sides of the piston. By multiplying the pressure difference with the effective cross-section area of the piston, the damping force was calculated based on the pressure data. This was then compared with the damping force measured with the load cell of the test setup. By comparing these two results, it was assumed that the difference between two force responses was caused by friction in the seals and the sliding bushings. After analysis of the force difference, the following friction force function was obtained:
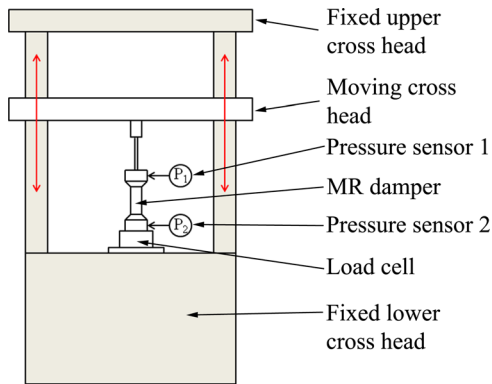
Fig. 6 Stress–strain machine setup to analyze quasi-static and dynamic properties of the MR damper

Fig. 8 Measured and simulated damping force responses of the magnetorheological damper of the compliant foot as a function of the electric current

$$F\mu(I) = 21.8 \text{ N/A} * I + 17 \text{ N} \tag{19}$$

where I is the applied electric current.

4.3 Quasi-Static Performance. In one quasi-static performance measurement, the damper was compressed and extended five times at a constant velocity and electric currents from 0 to 2 A were supplied. From the measured results, the constant velocity and the mean constant force were calculated resulting in five vertical force points in positive and negative directions for the static characteristic curves. This measuring procedure was repeated 60 times with different velocities in order to identify the quasi-static performance of the developed MR damper. The characteristic curves are presented in Fig. 7.

To simulate the quasi-static force responses by Eq. (17), the friction force at certain electric current was obtained by Eq. (19) and the yield stress of the MR fluid was estimated by the FEMM model. The measured characteristic curves and simulated responses are compared in Fig. 7.

Based on the results shown in Fig. 7, the dynamic range of the damper can be approximated by using Eq. (18). The ratio between the controllable and uncontrollable force at a speed of 60 mm/s results in a value of 14.9, which indicates of the controllability of the damping force in a wide range. In the development process of a MR damper application, the dynamic range can be considered as a design parameter and can vary from 2 to 25 depending on the target of the application [20–22]. In this study, the dynamic range
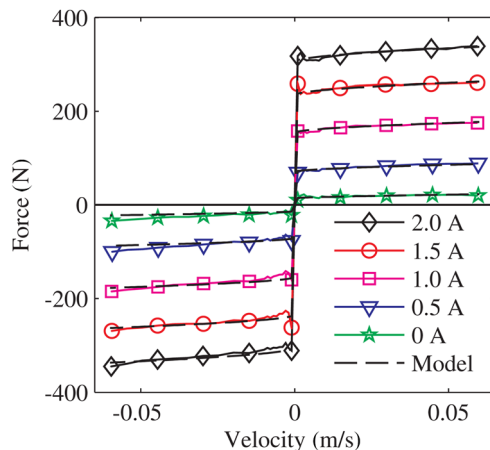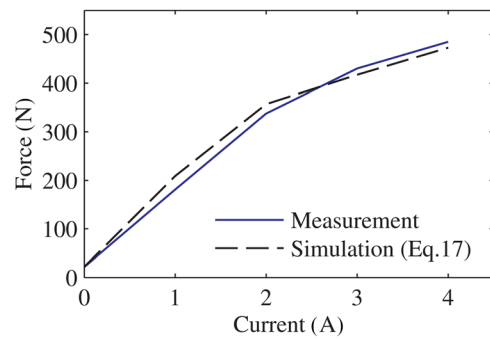
is a trade-off between the maximal force, light weight structure and the fluid flow path design and can be considered as a successful value.

4.4 Simulation of the Force Response. The force response of the damper was also simulated and measured as a function of the applied electric current. In these measurements, the damper was compressed at a constant velocity of 40 mm/s and electric currents from 1 to 4 A were applied with an increment of 1 A. The measured damping force is compared with the simulated response and the results are presented in Fig. 8.

The simulation of the damping force begins by creating a finite element (FE) model of the magnetic circuit of the MR device. Subsequently the yield stress of the MR fluid for different positions inside the fluid gap (and surroundings) can be estimated by combining the FE results of the magnetic field strength (Fig. 4) with the yield stress characteristic curve (Fig. 1) of the MR fluid. In the next step, the yield stress results of the MR fluid in the fluid gap are combined with Eq. (16) and by integrating over the length of the piston, the total pressure difference over the piston can be estimated. In many cases, sufficient accuracy is achieved when the pressure difference caused by the MR effect is integrated over the fluid gap(s) in which the MR fluid is activated. However, in this analysis also, the middle part of the piston (position range between 5 mm and 15 mm in Fig. 4) must be taken into account because the magnetic flux begins to spread outside of the MR fluid gap after the core parts begin to saturate. In this step, one should also note that the height of the fluid gap is not constant but a function of the position over the length of the piston. The real fluid gap height was identified by measuring diameters of the manufactured piston at different positions. After integration of the pressure difference over the piston, and taking the effect of the friction forces into account by Eq. (19), the total damping force can be calculated by Eq. (17).

Figure 8 demonstrates that the model predicts the measured damping force with a satisfactory accuracy even if the damper operates in the range where the core parts begin to saturate (I > 2 A). In the operating range below 2 A, the damping force increases linearly which was found to match well with the intended design criteria presented in Sec. 3.1.

Fig. 7 Comparison of measured and simulated quasi-static force-velocity characteristics of MR damper for different electric current inputs (0–2 A)

4.5 Frequency Response Measurements. The purpose of the frequency response measurements was to study the bandwidth of the controllable damping force. In these measurements, the displacement of the compression and extension of the damper was always 30 mm and a constant compression/extension velocity of 30 mm/s was used. During one compression-extension-cycle, sinusoidal electric current excitation was applied with 2 A peak-to-peak value. The frequency band of the electric current ranged from 2 to 100 Hz with an increment of 2 Hz from one cycle to
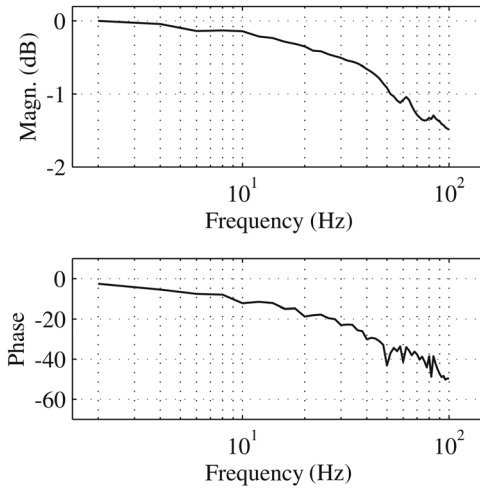
Fig. 9 Frequency response measurements of the damping force of the magnetorheological damper

another. The data sampling frequency was 1 kHz. The magnitude and phase curves of the frequency response measurement are presented in Fig. 9.

In the magnitude plot of Fig. 9, the 0 dB level can be estimated to correspond to a force of 340 N. The frequency response measurement was limited to 100 Hz, because it was estimated to be sufficient for this robotic application. Results for magnitude and phase manifest that boundary frequency is at higher than 100 Hz level. Based on these frequency response measurements, it can be concluded that the MR damper is able to be controlled up to the desired frequency.

5 Robotic Leg With the Magnetorheological Compliant Foot

This section describes the robotic setup chosen to test the effectiveness of the MR compliant foot. In this setup, the MR compliant foot was mounted onto the lower part of a robotic leg forming an additional prismatic joint to the leg mechanism. The leg (henceforth known as HyQ leg) was designed for a hydraulically actuated quadruped robot called HyQ, which is a scientific platform to study and develop the locomotion of four-legged robots. The specifications of the HyQ leg and HyQ can be found in Ref. [12]. Further on, the leg mechanism was mounted on a slider arrangement that allows only vertical movement of the leg and therefore the vertical bouncing dynamics of the leg mechanism can be studied. The experimental setup is presented in Fig. 10 with a functional description of the components.

The hydraulic actuators of two sagittal joints (hip and knee) were replaced with stiff aluminum rods in order to avoid the influence of the oil compliance in this study. The aluminum support rods were cut to certain length to obtain a configuration ($q_1 = -12$ deg and $q_1 = 24$ deg, see Fig. 11(b) for definition) to have the foot tip located under the hip axis.

In this experimental setup, the compression of the foot spring was measured by a linear potentiometer (Burster 8709) and an Austrian Microsystems (AS5045) absolute encoder connected to a steel cable and pulley system was used to define the vertical position of the slider. Ground reaction forces were acquired by means of a three-axis force plate (Kistler 9260AA6). The sampling rates of the data acquisition and the control loop frequency were set to 1 kHz. The whole leg structure (including the MR foot and the slider carriage) has a total weight of 7 kg. The spring in the compliant foot was chosen to have a spring constant of 15,800 N/m. This value was selected to achieve maximum compression (0.034 m) when the leg is dropped from a height of 0.3 m.
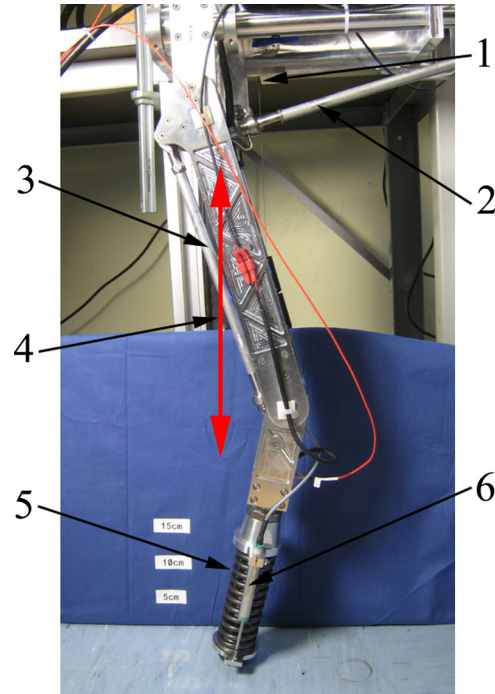

Fig. 10 Picture of the HyQ robotic leg with the magnetorheological compliant foot attached to a vertically sliding test setup: (1) slider position encoder, (2) hip support, (3) knee support, (4) slider guide, (5) magnetorheological compliant foot, and (6) foot compression sensor

6 End-Effector Stiffness for the Leg Mechanism

The configuration of the leg (without aluminium rods) is defined in the joint space by two rotational degrees of freedom and one linear degree of freedom. The leg configuration may have a strong influence on the stiffness and the damping characteristics at the end-effector level. In particular, the damping force acts in the direction of the longitudinal axis of the lower leg segment (joint space), while the bouncing requirements are defined at the leg end-effector level (task space). Therefore, it is necessary to define the mapping of the stiffness from the joint space to the task space. Given the vector of joint displacements

$$q = \begin{bmatrix} q_1 & q_2 & q_3 \end{bmatrix} \tag{20}$$

where the vector q is defined by the angular joint displacements of the hip (q_1), the angular joint displacements of the knee (q_2) and the linear displacement (q_3) in the compliant foot. The joints' stiffness tensor K_j is defined as the partial derivative of the joint torques τ with regard to the joint displacements q. By expanding the torque derivative using kineto-static duality [23] it is obtained

$$K_j = \frac{\partial \tau}{\partial q} = \frac{\partial (J^T f)}{\partial q} = \frac{\partial J^T}{\partial q} f + J^T \frac{\partial f}{\partial x} \frac{\partial x}{\partial q} \approx J^T K_t J \tag{21}$$

where J is the foot Jacobian matrix from the joint space to the task space (foot), f is the end-effector force vector, K_t is the task space (end effector) stiffness tensor and the instantaneous changes of the Jacobian with the configuration have been neglected. By rearranging Eq. (21), the end-effector stiffness tensor can be obtained

$$K_t = J^{+T} K_j J^+ \quad K_t = \begin{bmatrix} k_{xx} & k_{xy} \\ k_{yx} & k_{yy} \end{bmatrix} \tag{22}$$

As J is a rectangular 2×3 matrix the Moore-Penrose pseudoinverse J^+ has been selected for the inversion. In this study, since
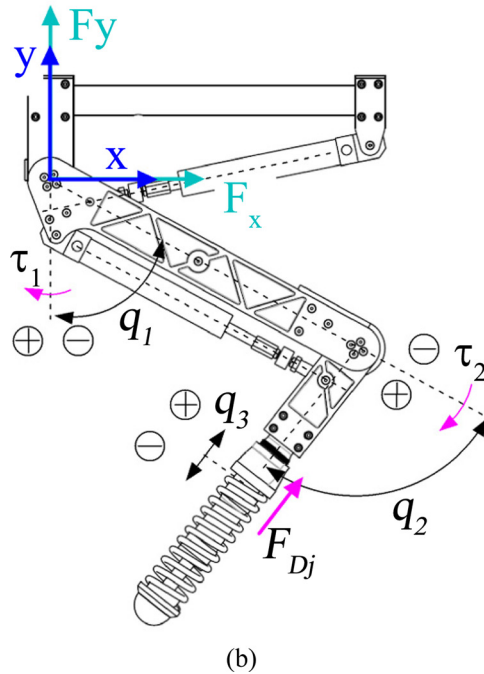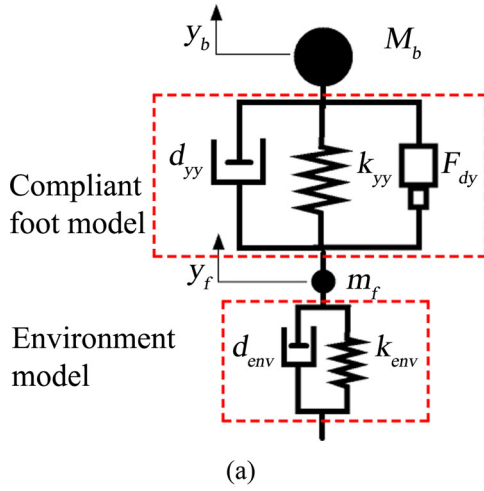
(a)

(b)

Fig. 11 (*a*) **Spring-mass-damper equivalent of the robotic leg and** (*b*) **joint and task space coordinates of the degrees of freedom and forces**

the movement of the hip/knee joints is fixed by aluminium rods, the only significant contribution to the leg compliance is due to the compliant foot and the other two links can be considered as a single rigid body. However, when the rods are replaced with hydraulic actuators, the first two terms on the diagonal of K_j matrix will represent the oil compressibility and the hose compliance in the hydraulic system.

7 Mathematical Modelling

A lumped parameter mathematical model of the leg has been built up for the identification of the end-effector stiffness and the passive damping (e.g., due to joint friction) of the leg. Further on, the model will be used in the development of the control laws.

7.1 The Dynamic Model of the Leg. During the stance phase the leg can be modelled as a spring-mass-damper system as illustrated in Fig. 11(*a*). The dynamic model of the leg is based on the estimation of the total forces on the different bodies of the leg and the projection of the forces in the *y*-direction of the end-effector.

Because of the presence of the aluminium rods, the masses of the links have been lumped into one mass (henceforth called body mass) m_b with sprung mass of 6.9 kg, whereas the foot mass m_f is defined by the mass of the foot tip located after the spring unsprung mass of 0.1 kg. As a result, two second order equations would be necessary to describe the dynamics of the masses m_b and m_f. However, since $m_b \gg m_f$, the model can be simplified to

$$\begin{cases} \ddot{y}_b \quad \text{flight} = -g \\ \ddot{y}_b \quad \text{stance} = -g + \frac{1}{m_b}\left(-k_{yy}(y_b - L_0) - d_{yy}\dot{y}_b + F_{Dy}\right) \end{cases} \quad (23)$$

where y_b is the body vertical displacement, $\dot{y}_b$ is the body vertical velocity, $\ddot{y}_b$ flight is the body vertical acceleration during the flight phase, $\ddot{y}_b$ stance is the body vertical acceleration during the ground contact phase, L_0 is the length of the MR compliant element when there is no foot spring compression, g is gravity, k_{yy} and d_{yy} are the end-effector stiffness and the passive damping of the system in the *y*-direction, and F_{Dy} is the MR damper force projected in the *y*-direction. During the flight phase, the only active force is gravity field.

7.2 Online Stiffness Identification. Online identification is useful when the stiffness of the ground changes. By identifying the ground stiffness, the parameters of the controller can be adapted accordingly and the performance of the semi-active damping can be optimized. The idea behind the online stiffness identification is that the natural frequency of the system does not change if the dynamics of the leg is described in the task space or in the joint space. However, the vertical position information of the slider encoder would not be available on a robot moving freely in the 3D space; a reliable estimate of the natural frequency can be obtained by using the measurements of the spring displacement. In this method, the spring compression time Δt and the maximum spring compression is measured every time the legs lands on the ground. The measuring sequence is illustrated in Fig. 12.

$$T = 4\Delta t \Rightarrow \omega_d = \frac{2\pi}{4\Delta t} = \omega_n^2 \sqrt{1 - \varsigma^2} = \sqrt{1 - \frac{d_{yy}^2}{4k_{yy}m_b}} \quad (24)$$

where ω_n is the angular frequency of the undamped oscillation. If the body mass m_b and the damping d_{yy} is known (after earlier identification), the end-effector stiffness k_{yy} can be estimated by

$$\omega_n = \sqrt{\frac{k_{yy}}{m_b}} \Rightarrow \omega_d^2 = \frac{k_{yy}}{m_b} - \frac{d_{yy}^2}{4m_b^2} \Rightarrow k_{yy} = m_b\omega_d^2 + \frac{d_{yy}^2}{4m_b} \quad (25)$$
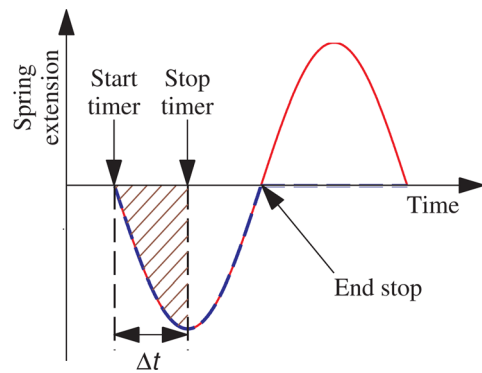

Fig. 12 **Damped response of a second order spring-mass-damper system (solid), compression of the spring after the impact (dashed). Once the spring has recovered its rest length a mechanical end-stop prevents further extension.**

Note that the k_{yy} stiffness also includes the ground stiffness. If the leg lands on a soft surface this ground compliance will be added in series to the foot reducing the overall compliance and resulting in lower forces that will build up for a longer time. This will result in a longer time Δt to decelerate completely the body mass and achieve the maximum leg compression. The outcome of this algorithm for estimating the stiffness by the compression time is a value that includes all the sources of compliance that can affect the mass dynamics (e.g., ground and joint stiffness) without having to estimate them separately. Furthermore, the fact that the estimation is performed at each bouncing step enables the system to efficiently adapt to different ground surface stiffness.

8 Control Algorithms

The main goal of the control law proposed in this section is to eliminate the bouncing of the leg during the ground contact and therefore improve the traction between the foot tip and the ground. As a secondary goal, the impact forces transmitted to the torso can be to reduce by semi-active control of the damping force.

8.1 Critical Damping Law. In order to attain a critically damped response for the robotic leg, a control law is proposed (in the task space) whereby a damping force is controlled as a combination of a virtual negative spring and a virtual damping element. The damping force F_{Dy} (expressed in the vertical direction y), can be formulated as

$$F_{Dy} = \alpha(y_b - L_0) - \beta \dot{y}_b \qquad (26)$$

where α is the negative spring constant and β is the virtual damping coefficient, while $y_b - L_0$ represents the extension/compression of the compliant foot in the task space. Furthermore, by combining Eq. (26) with Eq. (23) and using the notation defined in Fig. 11(b), the vertical dynamics is described by

$$m_b \ddot{y}_b + (k_{yy} - \alpha)(y_b - L_0) + (d_{yy} + \beta)\dot{y}_b = -m_b g \qquad (27)$$

In Eq. (27), the end-effector stiffness k_{yy} can be estimated by the online identification during the antecedent compression phase, whereas d_{yy} is obtained by identification tests.

The controller has two degrees of freedom: α and β. The influence of these parameters on the damped natural frequency ω_d and on the damping factor ξ of the system is described by Eq. (30). The parameter α can be chosen according to the desired settling time. A higher value of α will result in a more compliant leg and this will also reduce the forces transmitted to the torso because the energy stored in the spring is dissipated over a longer time interval. On the other hand, if the goal is to damp the oscillation over a shorter time, a lower value of α must be set. The parameter β must be set accordingly to obtain a critically damped response ($\xi_{crit} = 1$) (see Eq. (28)). In this situation, no overbounce should occur.

$$\omega_n = \sqrt{\frac{k_{yy} - \alpha}{m_b}} \quad \xi_{crit} = \frac{\beta + d_{yy}}{2m_b\omega_n} = \frac{\beta + d_{yy}}{2\sqrt{m_b(k_{yy} - \alpha)}} \qquad (28)$$

The parameters α and β in Eq. (28) are defined in the end-effector space and must be mapped into the joint space because the controllable damping force F_{Di} is expressed along the foot joint q_3. This mapping makes use of the Jacobian matrix, inverting Eq. (22)

$$A_j = J^T \begin{bmatrix} 0 & 0 \\ 0 & \alpha \end{bmatrix} J \quad B_j = J^T \begin{bmatrix} 0 & 0 \\ 0 & \beta \end{bmatrix} J \quad \alpha_j = A_{j(3,3)} \quad \beta_j = B_{j(3,3)}$$
$$F_{Dj} = \alpha_j q_3 - \beta_j \dot{q}_3 \qquad (29)$$

where F_{Dj}, α_j, and β_j are the controllable damping force and control parameters expressed in the joint space and q_3 and $\dot{q}_3$ are the foot spring displacement and velocity, respectively. To generate

F_{Dj} electric current must be driven through the coil of the MR damper according to the damper force characteristic depicted in Fig. 8.

9 Experimental Results

This section presents experimental results of the ground stiffness and damping identification and the responses of the critical damping control law for different values α of the negative spring.

During the elongation phase of the compliant foot, the total damping force must always be lower than the spring force to prevent the elongation stopping before the maximum extension of the foot spring. This suggests the convenience to express α as a fraction of the k_{yy} stiffness according to Eq. (30) by introducing the k_{ratio} variable

$$\alpha = \frac{k_{ratio} k_{yy}}{100} \qquad (30)$$

9.1 Stiffness and Damping Identification. The stiffness k_{yy} and passive damping d_{yy} of the system in y-direction were identified by drop tests when the controller was not active (only passive damping was present). During these tests, the leg mechanism was dropped from a height of 0.3 m onto very stiff ground, in which case it was assumed that no compliance was added from the environment. Equation (23) was fitted to the measured data in order to estimate the stiffness and passive damping parameters. The identified parameters are $k_{yy} = 19{,}000$ N/m and $d_{yy} = 226$ N/(m/s) which are also used in the implementation of the control law.

Test results (Fig. 13) show that without any control action, the leg bounces three times with a maximum bounce of 40 mm when the leg is dropped from the height of 0.3 m.

9.2 Results of the Critical Damping Law. The effectiveness of the proposed control law was studied by dropping the leg from the heights of 0.1 m, 0.2 m, and 0.3 m. The tests were performed with different values of the parameter k_{ratio}. The slider displacement y_b and the virtual damping force F_D responses were acquired. The results of the three drop heights are shown in Figs. 14–16, respectively. In all figures, the slider displacement zero-level corresponds to the level of the ground and the time line starts at the moment of touchdown.

The performance indexes used to evaluate the control law are the percentage bounce reduction %BR and the settling time t_s. The first criterion is defined as the percentage ratio between the overshoot and the steady settling value, and the second criteria is defined as the time elapsed from the instant of maximum compression to the instant in which 99% of the steady settling value is reached.

For example, with $k_{ratio} = 0$, there is no virtual spring effect and only virtual damping, and a bounce of 0.01 m for 0.3 m drop was
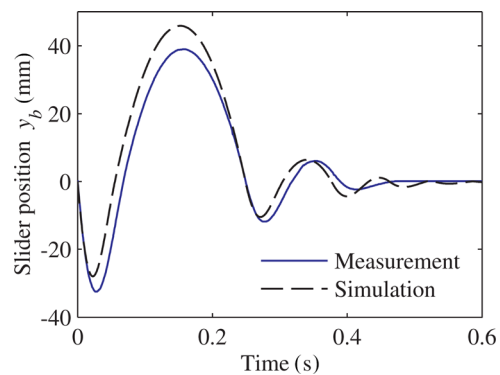

Fig. 13 Drop test (0.3 m) for identification of k_{yy} and d_{yy}. Simulation with the identified parameters is illustrated with dashdot line and measured response with solid line.
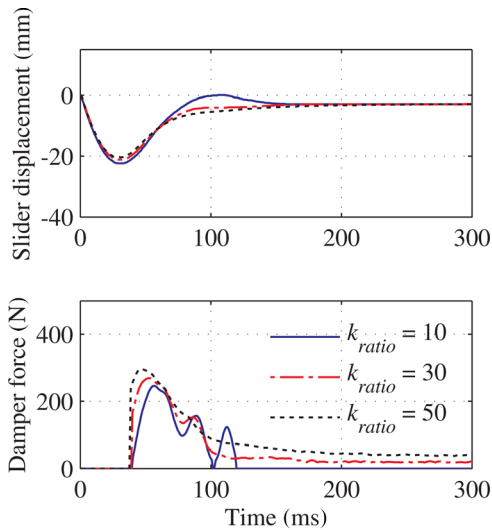
Fig. 14 Critical damping law for the 0.1 m drop test with k_{ratio} = 10 (solid), 30 (dashed–dotted), 50 (dotted): first plot slider displacement, second plot damper force
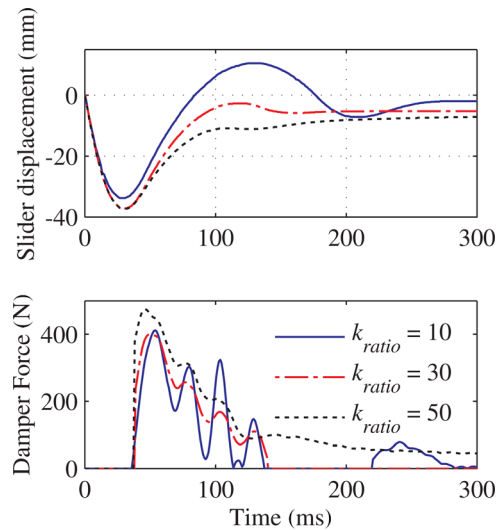

Fig. 16 Critical damping law for the 0.3 m drop test with k_{ratio} = 10 (solid), 30 (dashed–dotted), 50 (dotted): first plot slider displacement, second plot damper force
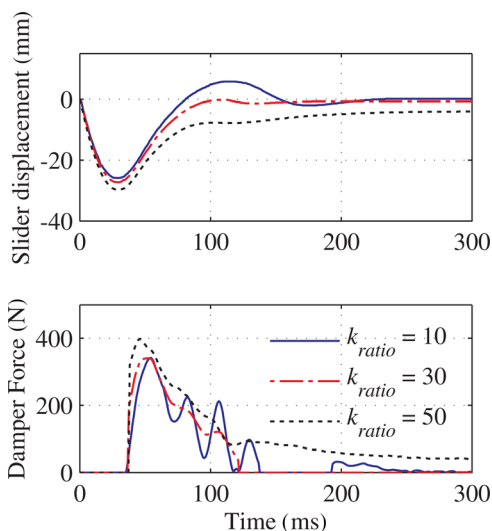

Fig. 15 Critical damping law for the 0.2 m drop test with k_{ratio} = 10 (solid), 30 (dashed–dotted), 50 (dotted): first plot slider displacement, second plot damper force

Table 2 Bouncing reduction performance for different values of k_{ratio}

Parameter	Drop height (m)	Test 1			Test 2		
		k_{ratio}			k_{ratio}		
		0	30	50	0	30	50
% BR	0.1	81	100	99	83	100	100
t_s (ms)		230	180	215	170	180	260
% BR	0.2	78	98	99	72	98	100
t_s (ms)		230	170	280	250	190	250
% BR	0.3	63	92	99	61	92	100
t_s (ms)		260	180	250	260	190	230

down. The repeatability of the experiment in terms of bouncing reduction was performed with a maximum error of 2%.

achieved. This corresponds to a bounce reduction of 63%. With k_{ratio} = 30 and k_{ratio} = 50, results are better. Table 2 compares the performance of the above mentioned experiments. The tests have been repeated twice to prove the repeatability of the results.

Table 2 shows that with k_{ratio} = 50, the best performance in terms of bounce reduction for every drop height (99%) was achieved, but on the other hand, a higher k_{ratio} causes a generally higher settling time that varies from 215 ms to 280 ms. The average settling time t_s is approximately 180 ms and 250 ms for k_{ratio} = 30 and k_{ratio} = 50, respectively. As expected, a higher k_{ratio} results in higher α values and therefore longer settling times. Theoretically, settling time for an oscillatory system is independent of the dropping height and can be estimated as $t_s = 4.6/\omega_n\xi$ [24]. Calculating ω_n by Eq. (28), the settling time should be 110 ms and 130 ms for k_{ratio} = 30 and k_{ratio} = 50, respectively, and this fits with the experimental results in Fig. 16 (upper plot). Within the performed set of experiments, the best trade-off between settling time and bounce reduction was obtained with k_{ratio} = 30. For k_{ratio} = 0, the higher settling time, it is due to the fact that there is no virtual stiffness force and the oscillations take longer to settle

10 Conclusions

This paper presented the design, model, and experimental evaluation of the performance of a novel compliant foot for a quadruped robot. The compliance of the robotic foot was achieved by use of a linear spring and magnetorheological technology. MR fluids make it possible to integrate a semi-active damper into the foot structure in which case the damping force of the compliant foot can be controlled in real-time during single ground contact, thus improving the traction of the foot.

The performance of the MR damper was analyzed from the quasi-static and dynamic point of view and a third order analytic model of the MR damper was found to fit to the static characteristic curve with a good correlation between the model and measured data. As a static performance, the damping force was able to be altered in a range of 15–310 N at low velocities and at the maximum measured speed of 60 mm/s, the dynamic range was calculated to be a factor of 14.9 between the total damping force and uncontrollable damping force. The achieved dynamic range can be considered as an indication of the controllability of the damping force over a wide range that is useful for robotic applications. The dynamic performance of the damper was studied by using sinusoidal current excitation to define the operating bandwidth of the MR damper. As a result, the − 3 dB level of the damping force

was found beyond 100 Hz proving the damper can be used in real-time control applications.

In the control application, the performance of the magnetorheological compliant foot was estimated by drop-test experiments. In these, the robotic leg with the compliant foot was fixed on a vertically sliding test setup that allowed one degree of freedom movement for the leg and allowed a reproducible test environment. The aim of these experiments was to study how the chatter between the foot tip and the ground could be avoided by integrating a semi-active damping element into the compliant foot of a robotic leg. A critical damping law has been proposed whereby the damping force of a compliant foot is controlled by a combination of a negative spring and a virtual damping element.

The aim of the semi-active damping was to dissipate all the kinetic energy during the first ground contact sequence. An algorithm was proposed to identify the end-effector stiffness (including the environmental surface stiffness) during the compression phase. This allowed the controller to adapt its parameters to different ground surfaces, which the robot may move on.

The performances of the control law for different dropping heights were assessed by experimental tests using bounce reduction %BR and settling time t_s as a performance criteria. The best trade-off between the settling time and the bounce reduction was found with $k_{ratio} = 30$ when 98%BR and 170 ms settling time can be achieved with medium drop height of 0.2 m.

Future works will test the effectiveness of the proposed approach with the hydraulic cylinders mounted on the leg. In that case, the hydraulic compliance will have to be included in the joint stiffness matrix and will affect the leg compliance. In addition, the constraint of the leg mounted on a vertical slider will be relaxed, considering the leg landing with different angles and postures. The use of an inertial measurement unit in conjunction with the joint encoders it is possible to estimate the position of the leg joints and end-effector in a world frame. An appropriate Jacobian matrix (that will include the body posture) will be used to map the joint movements to the end-effector movements (defined in the world frame) allowing the implementation of the proposed control law without any loss of generality.

Performance with different surfaces may be also investigated. Furthermore, four new magnetorheological compliant foots which are optimized for the HyQ robot, will be designed and manufactured in order to be able to study the semi-active compliance during walking and running.

Acknowledgment

References

[1] Robinson, D. W., Pratt, J. E., Paluska, D. J., and Pratt, G. A., 1999, "Series Elastic Actuator Development for a Biomimetic Walking Robot," Proceedings of IEEE/ASME International Conference on Advanced Intelligent Mechatronics, Atlanta, pp. 561–568

[2] Buchli, J., Kalakrishnan, M., Mistry, M., Pastor, P., and Schaal, S., 2009, "Compliant Quadruped Locomotion Over Rough Terrain," Proceedings of IEEE/RSJ International Conference on Intelligent Robots and Systems (IROS), St. Louis, pp. 814–820.

[3] Focchi, M., 2013, "Strategies to Improve the Impedance Control Performance of a Quadruped Robot," Ph.D thesis, Istituto Italiano di Tecnologia, Genoa, Italy.

[4] Pratt, G. A., and Williamson, M. M., 1995, "Series Elastic Actuators," Proceedings of IEEE—Int. Workshop on Intelligent Robots and Systems (IROS'95), Pittsburgh, PA., pp. 399–406.

[5] Tonietti, G., Schiavi, R., and Bicchi, A., 2005, "Design and Control of a Variable Stiffness Actuator for Safe and Fast Physical Human/Robot Interaction," Proceedings of IEEE—International Conference Robotics and Automation (ICRA'05), Barcelona, Spain, pp. 526–531.

[6] Hurst, J. W., Chestnutt, J., and Rizzi, A., 2004, "An Actuator With Mechanically Adjustable Series Compliance," Carnegie Mellon Robotics Institute, Technical Report No. CMU-RI-TR-24. (Available at http://www.ri.cmu.edu/pub_files/pub4/hurst_jonathan_w_2004_1/hurst_jonathan_w_2004_1.pdf)

[7] Chou, C.-P., and Hannaford, B., 1996, "Measurement and Modeling of McKibben Pneumatic Artificial Muscles," IEEE Trans. Rob. Autom., 12(1), pp. 90–102.

[8] Verrelst, B., Van Ham, R., Vanderborght, B., Daerden, F., and Lefeber, D., 2005, "The Pneumatic Biped LUCY Actuated With Pleated Pneumatic Artificial Muscles," Auton. Rob., 18(2), pp. 201–213.

[9] Klute, G. K., Czerniecki, J. M., and Hannaford, B., 2002, "Artificial Muscles: Actuators for Biorobotic Systems," Int. J. Rob. Res., 21(4), pp. 295–309.

[10] Chee–Meng, C., Geok–Soon, H., and Wei, Z., 2004, "Series Damper Actuator: A Novel Force/Torque Control Actuator," 4th IEEE/RAS International Conference on Humanoid Robots, Santa Monica, pp. 533–546.

[11] Laffranchi, M., Tsagarakis, N., and Caldwell, D., 2010, "A Variable Physical Damping Actuator (VDPA) for Compliant Robotic Joints," IEEE International Conference on Robotics and Automation (ICRA), Anchorage, Alaska, pp. 1668–1674.

[12] Semini, C., Tsagarakis, N. G., Guglielmino, E., Focchi, M., Cannella, F., and Caldwell, D. G., 2011, "Design of HyQ—A Hydraulically and Electrically Actuated Quadruped Robot," J. Syst. Control Eng., 225(6), pp. 831–849.

[13] Semini, C., 2010, "HyQ—Design and Development of a Hydraulically Actuated Quadruped Robot," Ph.D. thesis, Italian Institute of Technology and University of Genoa, Italy.

[14] Jalili, N., 2002, "A Comparative Study and Analysis of Semi-Active Vibration-Control Systems," J. Vib. Acoust., 124(4), pp. 593–605.

[15] Bossis, G., Lacis, S., Meunier, A., and Volkova, O., 2002, "Magnetorheological Fluids," J. Magn. Magn. Mater., 252, pp. 224–228.

[16] Goncalves, F. D., Ahmadian, M., and Carlson, J. D., 2006, "Investigating the Magnetorheological Effect at High Flow Velocities," Smart Mater. Struct., 15(1), pp. 75–85.

[17] Kostamo, J., Kostamo, E., Kajaste, J., and Pietola, M., 2008, "Magnetorheological (MR) Damper With a Fast Response Time," Proceedings of FPMC 2008, Bath, UK, pp. 169–182.

[18] Lord Corporation, 2009, "Magnetorheological Fluid MRF132DG," Product specification.

[19] Wilkinson, W. L., 1960, "Non-Newtonian Fluids: Fluid Mechanics, Mixing and Heat Transfer," London Pergamon, pp. 50–54.

[20] Mao, M., Young-Tai, W. H., and Wereley, N. M., 2007, "A Magnetorheological Damper With Bifold Valves for Shock and Vibration Mitigation," J. Intell. Mater. Syst. Struct., 18, pp. 1227–1232.

[21] Bass, B. J., and Christenson, R. E., 2007, "System Identification of a 200 kN Magneto-Rheological Fluid Damper for Structural Control in Large-Scale Smart Structures," Proceedings of American Control Conference, pp. 2690–2695.

[22] Nguyen, Q.-H., and Choi, S.-B., 2009, "Optimal Design of a Vehicle Magnetorheological Damper Considering the Damping Force and Dynamic Range," J. Smart Mater. Struct., 18(1), pp. 1–10.

[23] Siciliano, B., Sciavicco, L., Villani, L., and Oriolo, G., 2009, Robotics Modelling, Planning and Control, Springer, New York.

[24] Franklin, G. F., Powell, J. D., and Emami-Naeini, A., 1993, Feedback Control of Dynamic Systems, Addison-Wesley Longman Publishing, Boston, MA.